Available online at www.sciencedirect.com
ScienceDirect
Journal of the Mechanics and Physics of Solids
55 (2007) 64–90

JOURNAL OF THE MECHANICS AND PHYSICS OF SOLIDS

www.elsevier.com/locate/jmps

The nanogranular nature of C–S–H

Georgios Constantinides, Franz-Josef Ulm*

Massachusetts Institute of Technology, Cambridge, MA 02139, USA

Received 12 January 2006; received in revised form 11 June 2006; accepted 15 June 2006

Abstract

Despite its ubiquitous presence as binding phase in all cementitious materials, the mechanical behavior of calcium–silicate–hydrates (C–S–H) is still an enigma that has deceived many decoding attempts from experimental and theoretical sides. In this paper, we propose and validate a new technique and experimental protocol to rationally assess the nanomechanical behavior of C–S–H based on a statistical analysis of hundreds of nanoindentation tests. By means of this grid indentation technique we identify in situ two structurally distinct but compositionally similar C–S–H phases heretofore hypothesized to exist as low density (LD) C–S–H and high density (HD) C–S–H, or outer and inner products. The main finding of this paper is that both phases exhibit a unique nanogranular behavior which is driven by particle-to-particle contact forces rather than by mineral properties. We argue that this nanomechanical blueprint of material invariant behavior of C–S–H is a consequence of the hydration reactions during which precipitating C–S–H nanoparticles percolate generating contact surfaces. As hydration proceeds, these nanoparticles pack closer to center on-average around two characteristic *limit* packing densities, the random packing limit ($\eta = 64\%$) and the ordered face-centered cubic (fcc) or hexagonal close-packed (hcp) packing limit ($\eta = 74\%$), forming a characteristic LD C–S–H and HD C–S–H phase.

Keywords: C–S–H; Nanoindentation; Statistical methods; Granular material; Packing density

1. Introduction

No doubt, calcium–silicate–hydrate (C–S–H), the binding phase in all cementitious materials, is one of the most complicated and intriguing material systems in materials

*Corresponding author. Tel.: +1 617 253 3544; fax: +1 617 253 6044.
E-mail address: ulm@mit.edu (F.-J. Ulm).

0022-5096/$ - see front matter © 2006 Elsevier Ltd. All rights reserved.
doi:10.1016/j.jmps.2006.06.003

science and engineering. While several models coexist that describe the structural evolution of C–S–H at the crystal chemical level (for a recent review see Richardson, 2004), per today, the link between composition, nano- and microstructure *and* mechanical behavior of C–S–H is still an enigma that has deceived many decoding attempts. From atomic force microscope (AFM) investigations (Nonat, 2004), small angle neutron scattering (SANS) (Jennings et al., 2006) and transmission electron microscopy (TEM) (Richardson, 2004), there is now ample evidence that the elementary C–S–H particle is a nanoparticle whose smallest dimension is on the order of 5 nm. Depending on type and mode of observation, the opinions, however, differ as regards the other dimensions. To name a few: based on AFM measurements, Nonat (2004) suggests a brick-type morphology of the nanoparticle (lamellae) of dimension $60 \times 30 \times 5\,\mathrm{nm}^3$. From density, composition and surface area measurements, Jennings (2000, 2004) and Tennis and Jennings (2000) postulate a globular C–S–H particle morphology of characteristic size 5.6 nm, which includes an 18% nanoporosity. At larger scales, those globular particles agglomerate to form a low density (LD) and a high density (HD) C–S–H 'gel', that differ only in the gel-porosity. Based on TEM imagining of C_3S and C_2S pastes, Richardson (2004) attributes the globular particle morphology to the so-called inner product (Ip) C–S–H (which is 4–8 nm in size in pastes hydrated at 20 °C but smaller at elevated temperatures, 3–4 nm), from a fibrillar morphology of outer product (Op) C–S–H which consists of aggregations of long thin particles that are about 3 nm in their smallest dimension and of variable length, ranging from a few nanometers to many tens of nanometers.

Does morphology matter? This is the question that arises from those different observations–conjectures, and it is the question we want to address in this paper. To achieve our goal, we have developed a new technique based on the statistical analysis of hundreds of nanoindentation tests on cement paste. This technique builds on our previous nanoindentation analysis of highly heterogeneous composites (Constantinides et al., 2003; Constantinides and Ulm, 2004; Ulm et al., 2005), and carries it on to the next level to allow for identification and quantification of meaningful mechanical phase properties, volume fractions and morphology of multi-phase and multi-scale composites from first- and second-order statistical moments.

The paper is composed of two parts: we first present the novel grid-indentation technique and suggest a protocol how to perform such tests and analysis. This technique is applied to and thoroughly validated for C–S–H, to obtain key mechanical properties of C–S–H that should be helpful to identify the link between morphology and mechanical properties of C–S–H. The second part analyzes the experimental results from a micromechanics perspective and aims at identifying if and how morphology affects the mechanical nanoproperties of C–S–H.

2. Materials and methods

2.1. Nanoindentation on natural composites

It is now well established that the response of a material upon the reversal of contact loading provides access to the elastic properties of the intended material (for recent review see Oliver and Pharr, 2004; Cheng and Cheng, 2004). The indentation technique consists of establishing contact between an indenter of known geometry and mechanical properties (typically diamond) and the indented material for which the mechanical properties are of

interest, and subsequently acquiring the continuous change in penetration depth h as a function of increasing indentation load P ($P-h$ curve, see Fig. 1). Typically, the extraction of mechanical properties is achieved by applying a *continuum scale* mechanical model to derive two quantities, indentation hardness H and indentation modulus M:

$$H \stackrel{\text{def}}{=} \frac{P}{A_c}, \tag{1}$$

$$M \stackrel{\text{def}}{=} \frac{\sqrt{\pi}}{2}\frac{S}{\sqrt{A_c}}. \tag{2}$$

All quantities required to determine H and M are directly obtained from the $P-h$ curves, with the exception of the projected area of contact A_c. Chief among those are the maximum applied force P_{max} and corresponding maximum depth h_{max}, the unloading indentation stiffness $S = (dP/dh)_{h=h_{max}}$, and residual indentation depth h_f upon full unloading of the material surface (Fig. 1). The contact area A_c can also be extrapolated from the maximum depth h_{max}. Furthermore, M can be linked to the elastic constants of the indented material by applying a linear elastic model to the data (Galin, 1961; Sneddon, 1965). In the isotropic case, M reduces to the plane-stress elastic modulus,

$$M = \frac{E}{1-\nu^2} = 4G\frac{3K+G}{3K+4G}, \tag{3}$$

where E is the Young's modulus, ν the Poisson's ratio; G is the shear modulus and K the bulk modulus of the indented isotropic material. Similarly, the hardness H can be related to strength properties, namely the cohesion c and the friction angle φ, and the cone angle θ (Ganneau et al., 2006):

$$H = c\mathscr{F}(\varphi,\theta), \tag{4}$$

where $\mathscr{F}(\varphi,\theta)$ is a dimensionless function.

The methodology, however, is currently restricted to monolithic systems, and little has been reported for indentation on composite materials, a category composing the majority

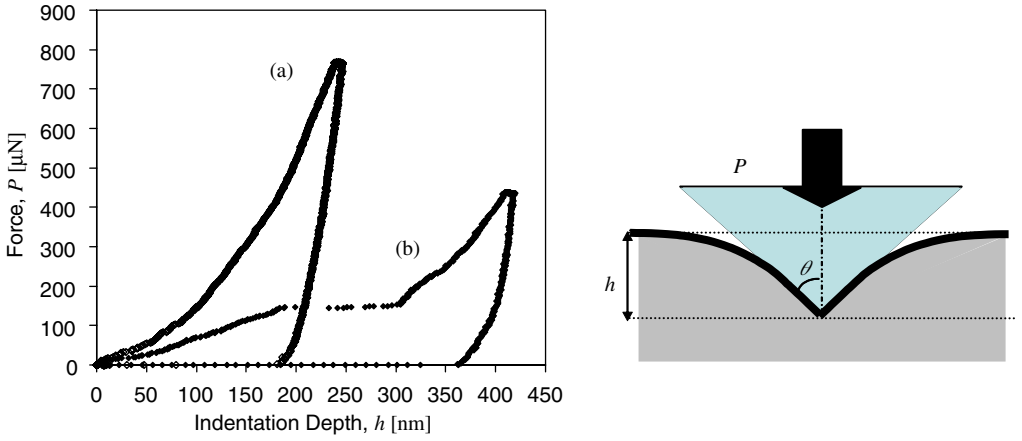

Fig. 1. Indentation force–indentation depth curves, $P-h$: (a) regular response satisfying self-similarity; (b) irregular response with jump in displacement due to fracture.

of solids. Application of Eqs. (1)–(4) to multi-scale composites poses several challenges, as the underlying contact mechanics analysis relies on the self-similarity of the indentation test on an infinite half-space. This strictly holds only for homogeneous materials that respect the separation of scale condition:

$$d \ll \mathscr{L} \ll h, \tag{5}$$

where $\mathscr{L}$ is the representative elementary volume (*rev*), which must be much greater than the size of the largest heterogeneity of size d contained in the *rev*; and much smaller than the indentation depth h, which defines the order of length magnitude of the strain gradient variation in the microstructure. The focus of the next sections is to show how this powerful technique can be employed for highly heterogeneous materials, like cement paste.

2.1.1. Gedanken experiment

Proposition 1. *Consider a material to be composed of two phases of different mechanical properties and characterized by a length scale D. If the indentation depth is much smaller than the characteristic size of the phases*, $h \ll D$, *then a single indentation test gives access to the material properties of either phase* 1 *or phase* 2. *If, in addition, a large number of tests* ($N \gg 1$) *is carried out on a grid defined by a grid spacing* ℓ *that is larger than the characteristic size of the indentation impression, so to avoid interference in between individual indentation tests, and much larger than the characteristic size of the two phases,* $\ell\sqrt{N} \gg D$, *so that the locus of indentation has no statistical bias with respect to the spatial distribution of the two phases, the probability of encountering one or the other phase is equal to the surface fraction occupied by the two phases on the indentation surface. On the other hand, an indentation test performed to a maximum indentation depth that is much larger than the characteristic size of the individual phases,* $h \gg D$, *senses the average response of the composite material, and the properties extracted from such an indentation experiment are representative in a statistical sense of the average properties of the composite material.*

This simple Gedanken experiment has all the ingredients of statistical indentation analysis that need to be performed when it comes to natural composite materials. The key results of such analysis are distributions and their derivatives (e.g., histograms or frequency diagrams) of mechanical properties determined by a large number of indentation experiments at a specific scale of material observation defined by the indentation depth. Generally speaking, small indentation depths, roughly $h/D < \frac{1}{10}$ (Buckle, 1973; Durst et al., 2004) provide access to mechanical phase properties, while greater indentation depths ($h/D > 6$) provide access to homogenized material properties of the composite. This principle is sketched in Fig. 2.

2.1.2. Deconvolution technique

The above Gedanken experiment is based on the premise that the two phases have properties of sufficient contrast so that those can be separated in small-scale indentation tests. Natural composite materials are generally more complex, requiring the use of some elementary statistics relations to analyze the indentation data. Let us assume that the distribution of the mechanical property $x = M, H$ of each phase J is best approximated by

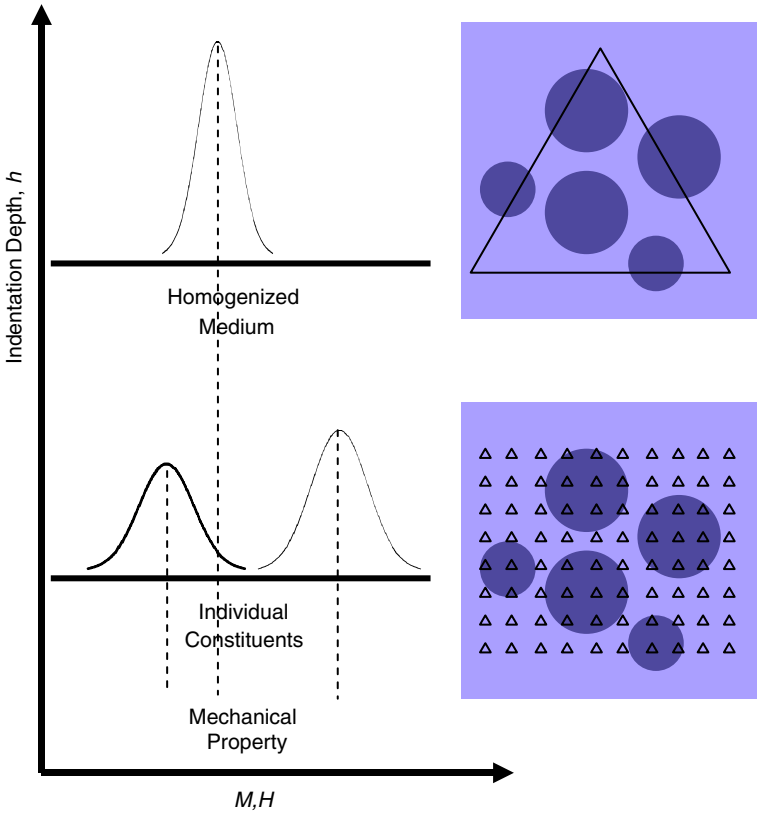

Fig. 2. Principle of statistical analysis of nanoindentation results. Small indentation depths allow the determination of phase properties, while larger indentation depths lead to the response of the homogenized medium.

the normal or Gaussian distribution:

$$p_J(x) = \frac{1}{\sqrt{2\pi s_J^2}} \exp\left(-\frac{(x-\mu_J)^2}{2s_J^2}\right), \tag{6}$$

where μ_J is the arithmetic mean of all N_J values of each phase, while the standard deviation s_J is a measure of the dispersion of those values:

$$\mu_J = \frac{1}{N_J}\sum_{k=1}^{N_J} x_k, \quad s_J^2 = \frac{1}{N_J - 1}\sum_{k=1}^{N_J}(x_k - \mu_J)^2. \tag{7}$$

The case of a single phase, $n = 1$, corresponds to the case of a homogeneous material (Fig. 2—top), for which mean value and standard deviation describe the properties of the material in a statistical sense. In the case of several phases ($J = 1, \ldots, n$), that all follow a normal distribution (Fig. 2—bottom), and which do not (mechanically) interact with each other, the overall frequency distribution of the mechanical property $x = (M, H)$ obeys to

the following *theoretical* probability density function:

$$P(x) = \sum_{J=1}^{n} f_J p_J(x), \tag{8}$$

where $f_J = N_J/N$ is the surface fraction occupied by phase J on the indented surface, which is subjected to the constraint:

$$\sum_{J=1}^{n} f_J = 1. \tag{9}$$

The problem so defined involves $3n-1$ unknowns; that is three unknown per phase, μ_J, s_J, f_J, reduced by the compatibility condition (9). If empirical frequency densities or response distributions are obtained by nanoindentation in form of discrete values P_i one can determine the unknowns by minimizing the standard error:

$$\begin{aligned} \text{Find } (\mu_J, s_J, f_J) \text{ from } \min \quad & \sum_{i=1}^{m} \frac{(P_i - P(x_i))^2}{m} \\ \text{s.t.:} \quad & \sum_{J=1}^{n} f_J = 1, \end{aligned} \tag{10}$$

where P_i is the observed value of the experimental frequency density; $P(x_i) = \sum_{J=1}^{n} f_J p_J(x_i)$ is the value of the theoretical probability density function shown in Eq. (8) at point x_i, and m is the number of intervals (bins) chosen to construct the histogram. The number of observed values P_i should exceed the number of unknowns, and must necessarily be smaller than the total number of tests N carried out on the surface; hence

$$3n - 1 \leqslant m < N. \tag{11}$$

2.1.3. A posteriori check of self-similarity

The deconvolution technique is based on the assumption that each individual indentation test respects the self-similarity of indentation in an infinite half-space. It is thus necessary to check a posteriori the relevance of this assumption by analyzing the dimensionless invariants of the indentation test. For conical indentation into an isotropic elastoplastic cohesive-frictional material, these are (Cheng and Cheng, 2004; Ganneau et al., 2006):

$$\frac{P}{Mh^2} = \Pi_\alpha\left(\frac{c}{M}, \nu, \varphi, \theta\right), \tag{12a}$$

$$\frac{A_c}{h^2} = \frac{P}{Hh^2} = \Pi_\beta\left(\frac{c}{M}, \nu, \varphi, \theta\right), \tag{12b}$$

where c/M is the cohesion-to-indentation modulus ratio, ν is the Poisson's ratio, φ is the friction angle, and θ is the half-apex angle of the conical indenter (Fig. 1). It is important to note that those invariant relations, because of the self-similarity of the indentation test, do not depend on any length scale, and in particular not on the indentation depth h. Therefore, plotting those invariants as a function of the indentation depth, provides an indirect means to check a posteriori the assumed self-similarity of the indentation data, and hence the scale separability condition (5).

2.2. Materials

2.2.1. Sample preparation

The material investigated here is a white cement paste. It is the same material tested by Thomas and Jennings (2002) for weight-loss experiments: white portland cement with a low aluminates content was cast into plastic molds at a water:cement ratio of $w/c = 0.5$, to form bars measuring $0.25\,\mathrm{m} \times 0.025\,\mathrm{m} \times 0.025\,\mathrm{m}$. The specimens were hydrated under limewater at room temperature and kept in such conditions until testing. For the indentation testing, the square plate specimens were cut into slices of approximate thickness 5–10 mm. The surfaces were prepared following standard procedures for SEM investigations of cementitious materials (Stutzman and Clifton, 1999): specimens were ground and polished with silicon carbide papers and diamond particles to obtain a flat and smooth surface finish. This was achieved in six stages of decreasing fineness with the last one being in the range of 250 nm. Such a smooth surface is of critical importance for nanoindentation tests, so to avoid introducing another length scale in the similarity analysis: the surface roughness. Polished surfaces were subsequently imaged using AFM and the average roughness and root mean square roughness were found to be on the order of 10–30 nm. Furthermore, special attention was paid to keep the specimens flat and parallel on both sides, since this could influence the angle of indentation, and thus the result of the measurements. After polishing, the samples were placed in an ultrasonic bath to remove the dust and diamond particles left on the surface or in the pore structure. The age of the material at testing was 5 months.

2.2.2. Choice of nanoindentation depth

Nanoindentation that focus on identifying phase properties, requires to choose the maximum indentation depth $h_{\max}$ so to respect on-average the scale separability condition (5) and the $\frac{1}{10}$ rule of thumb:

$$d \ll h_{\max} < \frac{D}{10}, \tag{13}$$

where d and D stand for the characteristic size of, respectively, the largest heterogeneity of the indented material and the microstructure. In the case of C–S–H, prime candidates for d are the single colloidal particle in C–S–H or the gel pores of similar size, $d \sim 5$ nm. On the other hand, the characteristic size of the microstructure D is more difficult to estimate, as the microstructure itself depends on mix proportions, hydration degree, etc. For a fully hydrated $w/c = 0.5$ cement paste, a good estimate of the characteristic length scale of the microstructure can be deduced from TEM images (Richardson, 2004) to be on the order of $D \sim 1-3\,\mu\mathrm{m}$, representing the smallest microstructural length scale among cement pastes' constituents (portlandite crystals and clinker particles are usually on the order of tens or hundreds of microns). Hence, an appropriate indentation depth that allows one to access the properties of the C–S–H phases by nanoindentation is

$$h_{\max} \in [100, 300]\,\mathrm{nm}. \tag{14}$$

For smaller depths, the indentation response will be affected by the discrete nature of the colloidal particles, and for larger depths the indentation response will be affected by the microstructure and the interaction of different phases. The order of magnitude of $h_{\max}$ also allows access to the in situ properties of portlandite (CH) and residual clinker phases if

present. Indeed, the elementary size of the portlandite crystal structure is on the order of $d = 0.5\,\text{nm}$ and the size D of crystals present in cementitious materials is on-average of micrometer dimension, which falls in the range of values covered by (14). We should emphasize, however, that (13) is only satisfied in an average sense, and that the presence of 'violators' of those conditions is inevitable. For instance, nanoindentation responses dominated by adjacent capillary voids of a characteristic size of 10–100 nm, fall in this category of indentation tests that do not satisfy the scale separability condition. On the other hand, within the context of the grid indentation technique, the error induced by indentation on such phases should be of random nature, and should be captured by the statistical analysis method.

Last, a convenient way to achieve the target indentation depth (14) is to employ a series of load-controlled indentation tests. This requires some experimental iterations. For the tested white cement paste, we found that a maximum load of roughly $P_{\max} = 500\,\mu\text{N}$ yields an average maximum indentation depth of $h_{\max} = 167 \pm 53\,\text{nm}$. In all indentation tests, a trapezoidal load history was prescribed, defined by a loading time $\tau_{\text{L}} = 10\,\text{s}$, a holding time of $\tau_{\text{H}} = 5\,\text{s}$, and an unloading time of $\tau_{\text{U}} = 10\,\text{s}$. In addition, a hold period of 20 s at the onset of unloading facilitated the correction for any thermal drift effects in the system.

2.2.3. Indentation data analysis

Prior to the application of the statistical method, the $P-h$ curves of all tests are inspected manually (visual inspection), in order to detect those that deviate from the theoretical $P \propto h^2$ scaling relation for conical or sharp indentation (see Eq. (12)). Such curves, as curve (b) in Fig. 1, which are a result of either improper contact detection or severe damage and fracture during loading, are easily detectable from their large (compared to the average value) recorded maximum penetration depth in the force driven indentation tests. They clearly violate the self-similarity of continuum indentation analysis and must be excluded from the statistical analysis. The largest percentage of discarded curves was related to surface preparation procedures, and the number of tests excluded for this reason was generally smaller than 5%. The rest of the indentation data were analyzed based on the tools of continuum indentation analysis: a function of the form $P = b(h - h_f)^m$ (where b, h_f, m are fitting parameters) is fitted to the unloading portion of each $P-h$ curve, and the indentation stiffness $S = (\text{d}P/\text{d}h)_{h=h_{\max}}$ is evaluated at maximum load $P_{\max}$. The indentation modulus M and the indentation hardness H are then calculated from (1) and (2), where the area of contact A_{c} at maximum load is estimated from the Oliver and Pharr (1992) method.

3. Nanoindentation results

3.1. Indentation modulus and hardness frequency densities

Figs. 3–5 display the experimental frequency distributions of the indentation modulus and the indentation hardness for three grid indentation experiments of 100 indents (10×10, grid spacing $\ell = 10\,\mu\text{m}$) performed with a Berkovich indenter on different sample areas (labeled N-1, N-2, N-3) of the same surface, together with fitted frequency distribution functions using the deconvolution technique. Fig. 6 displays the same for all 300 indentation tests. The three test series were carried out to study (1) the repeatability of the proposed test procedure and (2) the accuracy and convergence of the proposed

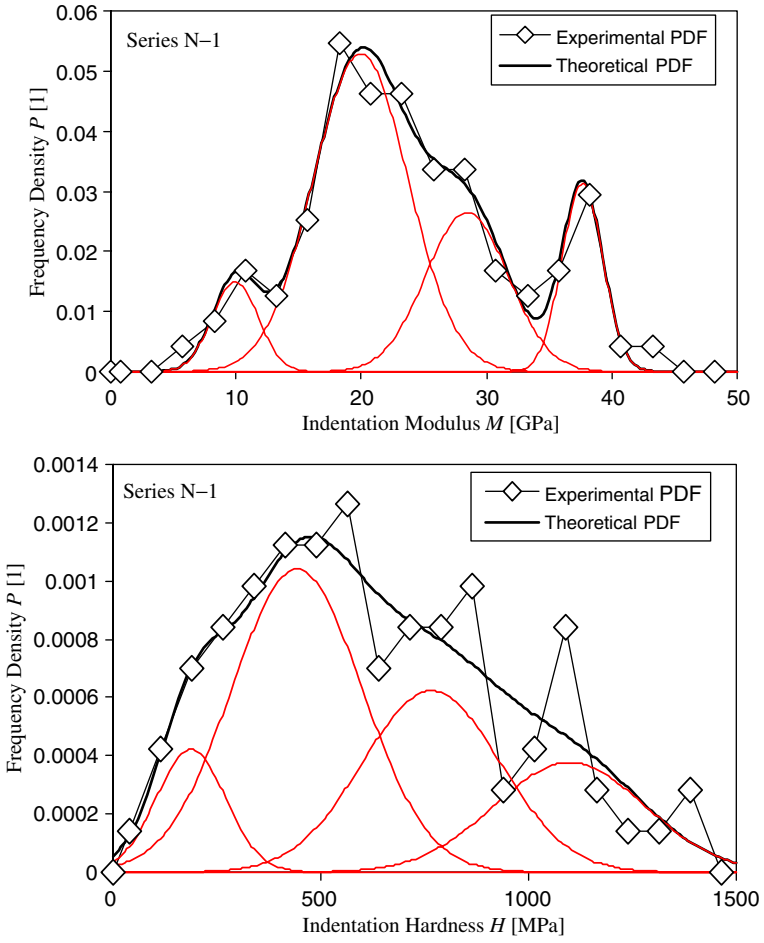

Fig. 3. Frequency plots of series N-1 (10×10 indentation tests on a grid of spacing $10\,\mu m$). The bin-size for deconvolution of the indentation modulus is $\Delta M = 2.5\,GPa$ and $\Delta H = 75\,MPa$ for hardness deconvolution.

deconvolution technique. Table 1 summarizes the derived quantities obtained by application of the deconvolution technique. In this application we sought for the minimum number of phases n required to represent the experimental frequency densities accurately. It turned out that $n = 4$ is sufficient to model the indentation data (M, H) on the $w/c = 0.5$ cement paste for indentation moduli $M \leqslant 50\,GPa$ and indentation hardness $H \leqslant 1.5\,GPa$. Values greater than $M = 50\,GPa$ and $H = 1.5\,GPa$ are attributed to indentation on residual clinker particles eventually present in the material, for which the indentation properties are known ($M \geqslant 125\,GPa$, $H \geqslant 8.0\,GPa$; Velez et al., 2001). Those higher stiffness and hardness values allow estimating the hydration degree from

$$\xi = 1 - \sum_{J=1}^{n=4} f_J, \tag{15}$$

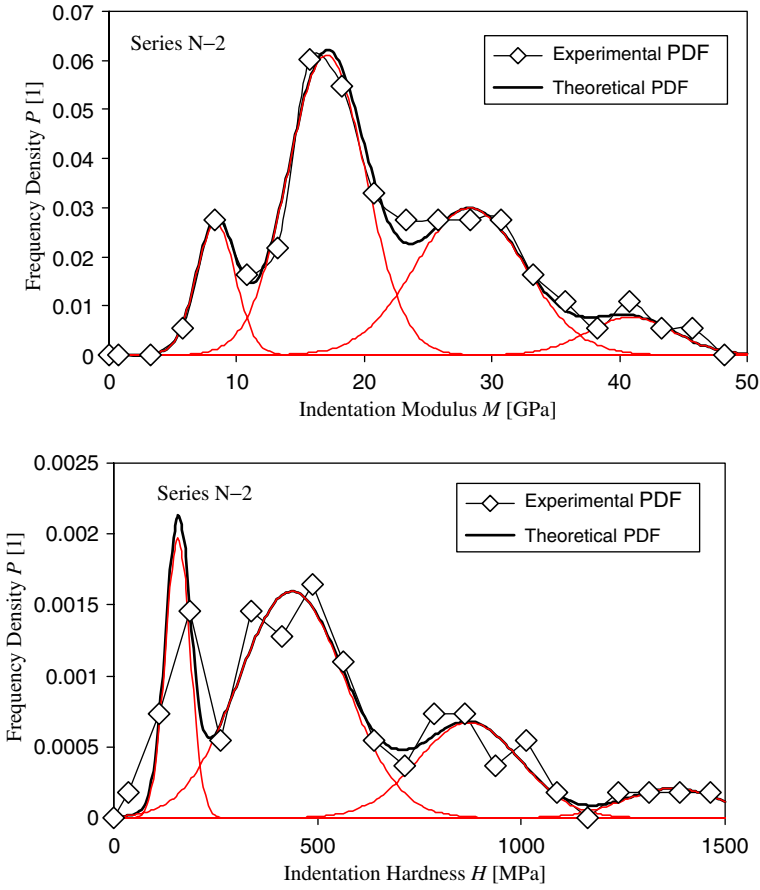

Fig. 4. Frequency plots of series N-2 (10×10 indentation tests on a grid of spacing $10\,\mu m$). The bin-size for deconvolution of the indentation modulus is $\Delta M = 2.5\,GPa$ and $\Delta H = 75\,MPa$ for hardness deconvolution.

where n are the four hydration phases detailed below. For the tested cement paste, the hydration degree so obtained is on the order of 94–95%, as one would expect from a well-hydrated (5 months old) $w/c = 0.5$ cement paste. The remaining four hydration phases from left (low stiffness/hardness) to right (high stiffness/hardness) are detailed below.

3.1.1. A low stiffness/hardness phase ('MP')

The lowest characteristic stiffness–hardness phase in Figs. 3–6 has a stiffness of $M = 8.1\,GPa$ and a hardness of $H = 0.17\,GPa$. We attribute those very low properties to material regions dominated by capillary pores. As stated before the indentation properties obtained for this phase should be handled with care, as the indentation data are often in violation of the scale separability condition required for the application of continuum indentation analysis. In return, considering those values in the deconvolution technique provides a means to estimate the volume fractions of the capillary pores; here (based on

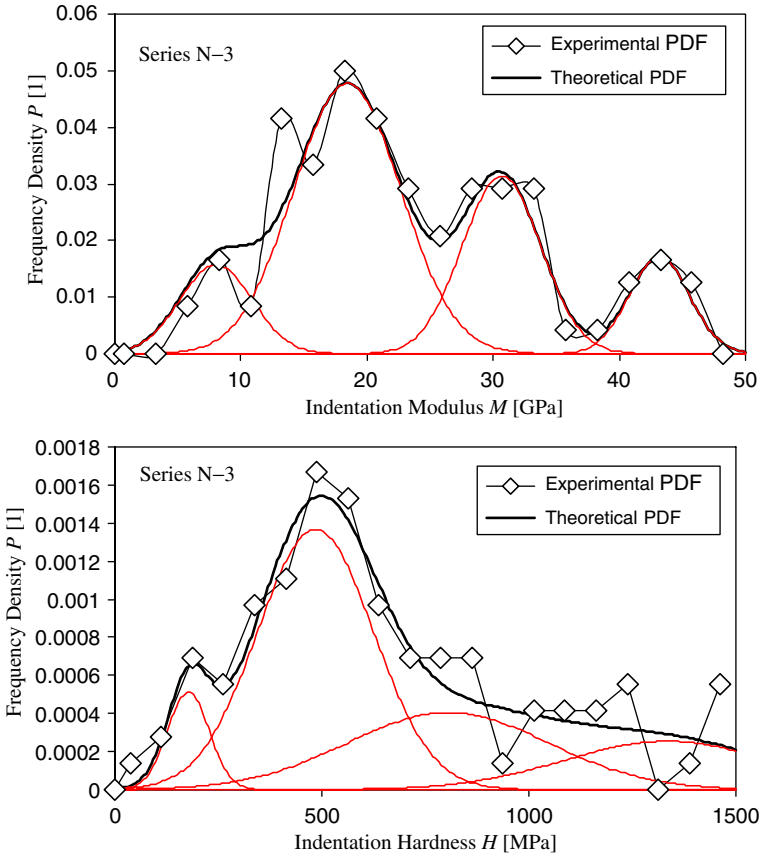

Fig. 5. Frequency plots of series N-3 (10×10 indentation tests on a grid of spacing $10\,\mu m$). The bin-size for deconvolution of the indentation modulus is $\Delta M = 2.5\,GPa$ and $\Delta H = 75\,MPa$ for hardness deconvolution.

300 indentation tests):

$$f_{MP} = 6{-}9\%. \tag{16}$$

The order of magnitude of the capillary porosity is consistent with Powers–Brownyard's semi-empirical relationship between macroporosity, initial w/c-ratio and degree of hydration ξ (Powers and Brownyard, 1948):

$$f_{MP}\left(\frac{w}{c} = 0.5, \xi = 0.95\right) = \frac{w/c}{w/c + 0.32}(1 + 1.32\xi) - 1.32\xi = 12\%. \tag{17}$$

Estimates provided by the deconvolution technique are expected to approach this value as the number of tests increases and the spacing between indents is reduced. There is, however, an inherent limitation to porosity determination from indentation that relates to the nature of the test itself. Each indentation commences upon contact detection through force measurements, and surface pores, therefore, cannot be sampled by indentation, unless the indenter touches the surface of the pore valley. One could

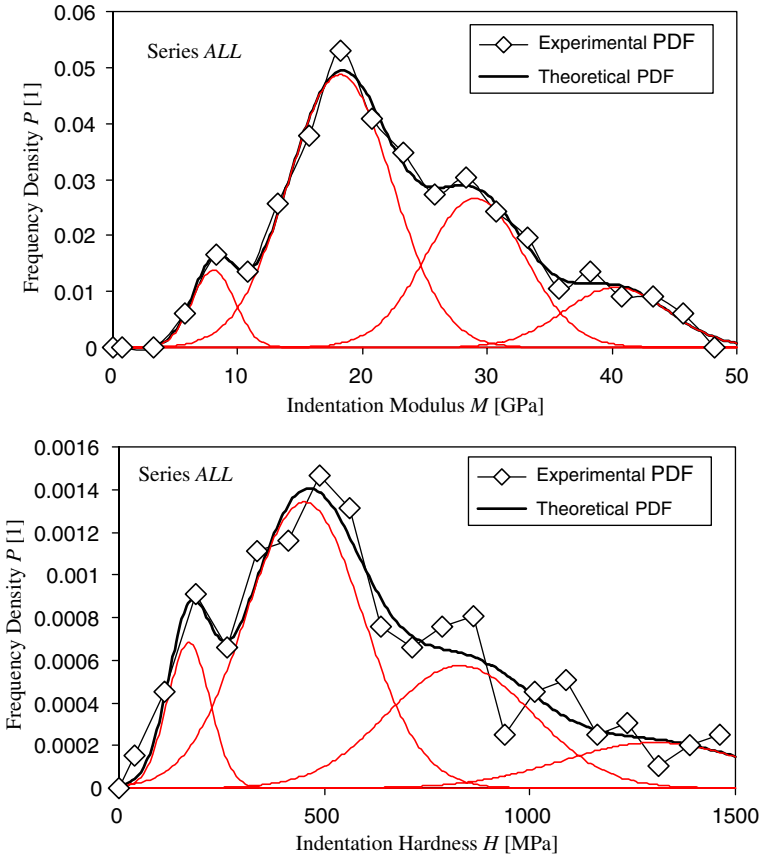

Fig. 6. Frequency plots of series N-1–N-3 (300 indentation tests). The bin-size for deconvolution of the indentation modulus is $\Delta M = 2.5\,\text{GPa}$, and $\Delta H = 75\,\text{MPa}$ for hardness deconvolution.

circumvent this drawback by impregnating the specimen surface with epoxy prior to testing, which might however compromise access to phase properties, as chemomechanical change during the impregnation process (for instance, C–S–H polymerization) cannot be excluded.

3.1.2. The low density C–S–H phase ('LD C–S–H')

The second peak in the frequency plots 3–6 is attributed to a LD C–S–H phase. Acker (2001) was the first to report values of $M = 20 \pm 2\,\text{GPa}$ and $H = 0.80 \pm 0.2\,\text{GPa}$ for a (calcium-to-silica ratio) $C/S < 1$ C–S–H phase in a $w/c = 0.2$ cementitious material. Constantinides et al. (2003) report $M_{\text{LD}} = 21.7 \pm 2.2\,\text{GPa}$ for a $w/c = 0.5$ cement paste, obtained by manually fitting Gaussian curves to the histogram. The stiffness values obtained here on the white cement paste with the (refined) deconvolution technique (300 values) are very much consistent with those values:

$$M_{\text{LD}} = 18.2 \pm 4.2\,\text{GPa}, \quad H_{\text{LD}} = 0.45 \pm 0.14\,\text{GPa}. \tag{18}$$

Table 1
Summary of grid indentation results for three different trials of 100 indentations obtained from a statistical analysis of the frequency diagrams: indentation modulus, hardness, volume fractions, and coefficients of variations for constituent phases

	[#]	P_{max} (μN)	h_{max} (nm)	Phase J	MP		LD C–S–H		HD C–S–H		CH	
				x	M	H	M	H	M	H	M	H
N-1	100	474 ± 10	170 ± 66	μ_J (GPa)	9.9	0.19	20.0	0.44	28.4	0.77	37.7	1.10
				$(s/\mu)_J$ (%)	18	45	19	35	12	22	4	16
				f_J (%)	7	9	50	41	22	26	13	17
N-2	100	469 ± 14	201 ± 90	μ_J (GPa)	8.4	0.16	17.1	0.44	28.3	0.87	40.9	1.37
				$(s/\mu)_J$ (%)	18	19	18	30	15	14	8	9
				f_J (%)	10	15	47	52	32	21	7	6
N-3	100	475 ± 12	176 ± 75	μ_J (GPa)	8.0	0.18	18.5	0.49	30.7	0.81	43.2	1.33
				$(s/\mu)_J$ (%)	36	28	23	29	10	30	6	19
				f_J (%)	11	6	51	48	25	25	10	16
ALL	300	473 ± 12	181 ± 77	μ_J (GPa)	8.1	0.17	18.2	0.45	29.1	0.83	40.3	1.31
				$(s/\mu)_J$ (%)	21	30	23	31	14	21	10	17
				f_J (%)	6	9	51	48	27	26	11	12

Table 2
Mass density reported by Jennings (2004), and derived packing density values of C–S–H at different scales

Scale	Density (kg/m^3)		Packing density
C–S–H solid	ρ_{sat}	ρ_{dry}	$\eta = 1 - \phi$
Basic building block	2800		1
C–S–H particle	2480	2300	0.82
C–S–H matrix			
LD C–S–H	1930	1440	0.63 ± 0.01
HD C–S–H	2130	1750	0.76 ± 0.02

ρ_{sat} and ρ_{dry} stand for the density, respectively, at full water saturation of the pore space and after oven-drying.

Note that the hardness value of the considered phase deviates from the value reported by Acker (2001) for a C–S–H phase having $C/S < 1$, which may simply be due to the fact that the C/S ratio of our $w/c = 0.5$ system is on-average higher; typically $C/S \sim 1.75$, which seems to affect the hardness of the LD C–S–H. In this system, the LD C–S–H is readily recognized to be the dominating phase. It makes up 65% of the total C–S–H volume, the rest being HD C–S–H. We obtained the same value of LD C–S–H in our previous investigation of a normal cement paste (not white cement paste) prepared at the same water–cement ratio of 0.5 (Constantinides et al., 2003). This value is also in excellent agreement with the empirical relationship of the LD C–S–H-to-total C–S–H mass ratio relation proposed by Tennis and Jennings (2000):

$$\mathscr{M}_r = \frac{m_{LD}}{m_{CSH}} = 3.017\frac{w}{c}\xi - 1.347\xi + 0.538 \tag{19}$$

which using known density values of the C–S–H phases (see Table 2)[1] translates into a LD C–S–H volume fraction of $V_{LD}/V_{CSH} = 62\%$.

3.1.3. The high density C–S–H phase ('HD C–S–H')

The third peak in the frequency plots 3–6 is attributed to a HD C–S–H phase. Acker (2001) reports $M = 31 \pm 4\,\text{GPa}$ and $H = 0.90 \pm 0.3\,\text{GPa}$ for a $C/S > 1$ C–S–H phase in a $w/c = 0.2$ cementitious material. Constantinides et al. (2003) report $M_{HD} = 29.4 \pm 2.4\,\text{GPa}$ for a $w/c = 0.5$ cement paste. Both values are in excellent agreement with the phase value we obtain here for the HD C–S–H phase in a $w/c = 0.5$ system (300 values):

$$M_{HD} = 29.1 \pm 4.0\,\text{GPa}, \quad H_{HD} = 0.83 \pm 0.18\,\text{GPa}. \tag{20}$$

3.1.4. Portlandite (CH)

The fourth peak in the frequency plots 3–6 is attributed to portlandite crystals dispersed in the cement paste matrix. Previous reported indentation properties for portlandite are $M = 36 \pm 3\,\text{GPa}$, $H = 1.35 \pm 0.5\,\text{GPa}$ (Acker, 2001) and $M = 38 \pm 5\,\text{GPa}$ (Constantinides and Ulm, 2004), which are in excellent agreement with the in situ values obtained in this investigation (300 values):

$$M_{CH} = 40.3 \pm 4.2\,\text{GPa}, \quad H_{CH} = 1.31 \pm 0.23\,\text{GPa}. \tag{21}$$

The estimated volume fraction of CH is

$$f_{CH} = 11-12\%. \tag{22}$$

It is instructive to compare this value with an estimate of CH volume fraction calculated on the basis of cement chemistry. For the given cement composition of the white cement paste having 72 wt% of C_3S (m_{C_3S}) and 17 wt% of C_2S (m_{C_2S}) the volume fraction of CH can be estimated from the stoichiometry of the chemical reactions (Ulm et al., 2004):

$$f_{CH} \simeq \frac{0.42\,m_{C_3S} + 0.13\,m_{C_2S}}{0.71 + 2.24\,w/c} \simeq 18\%. \tag{23}$$

While of the same order, the physical chemistry estimate (23) is higher than the one estimated from the grid indentation technique. There may be several reasons for this difference, one being that the physical chemistry expression is derived from the stoichiometry of CH-formation at complete hydration. But the most likely reason for this difference is the fact that CH crystals in cement pastes are large crystals that are irregularly dispersed throughout the microstructure. It is most likely that a greater number of indentation tests on a larger surface would allow a more accurate measure of the true CH crystal volume fraction.

[1] Indeed, a straightforward substitution of the mass of the saturated C–S–H particle (which includes an 18% nanoporosity) and of the water mass saturating the gel porosity yields the following expression for the LD C–S–H-to-total C–S–H volume ratio:

$$\frac{V_{LD}}{V_{CSH}} = \frac{\mathscr{M}_r(\rho_s\eta_{HD} + \rho_w(1-\eta_{HD}))}{\mathscr{M}_r(\eta_{HD}-\eta_{LD})(\rho_s-\rho_w) + \rho_s\eta_{LD} + \rho_w(1-\eta_{LD})},$$

where $\eta_{LD} = 64\%$ and 74% stand for the packing density of the LD C–S–H and HD C–S–H phase, respectively, while $\rho_s = 2480\,\text{kg/m}^3$ is the saturated mass density of the C–S–H particle, and $\rho_w = 1000\,\text{kg/m}^3$ is the water density (saturating the gel porosity). Noting that $\mathscr{M}_r(w/c = 0.5; \xi = 0.94) = 0.69$, we obtain a 62% LD C–S–H volume fraction.

3.2. Repeatability of grid indentation technique

The stiffness and hardness values in (18), (20) and (21) are mechanical properties of the LD C–S–H, HD C–S–H and CH phase obtained from the deconvolution of a total of 300 indentation tests performed on three different areas of the same surface. To study the accuracy and convergence of the grid indentation technique, Table 1 gives a detailed account of properties and volume fractions extracted with the deconvolution technique for each series (N-1, N-2, N-3), which calls for the following comments:

1. Mean values μ_J: The difference in mean values between different series is on the order or smaller than the standard deviation, and hence statistically insignificant. It is interesting to observe that the mean values obtained by deconvoluting the total number of tests (ALL) is not a simple average of the mean values of the three test series.
2. Standard deviation s_J/coefficient of variation $(s/\mu)_J$: The deviation of the mechanical properties of each phase from their mean values shows some variation between test series. The spread of the data for each phase, here quantified in terms of the standard deviation, respectively coefficient of variation $(s/\mu)_J$, is generally more pronounced for hardness than for the indentation modulus. This is a result of at least three phenomena: (i) the natural variability of each phase related e.g., to variability of the porosity, which affects strength properties and thus hardness in a more pronounced way than elasticity properties; (ii) the mechanical interaction between phases, which affects the hardness more than the indentation modulus; and (iii) possible errors in the estimation of the contact area A_c which affects the hardness $H \propto 1/A_c$ more than the indentation modulus $M \propto 1/\sqrt{A_c}$ (see relations (1) and (2)).
3. Volumetric proportions f_J: There is some variation in the volume fraction between test series, and this more for the volume fraction determined by deconvoluting the hardness frequency than for the volume fraction obtained by deconvoluting the stiffness frequency. In general, for volume fraction determination of the constituent phases one needs to sample a large enough area with closely spaced indents in order to converge to the actual values. Indeed, as the number of tests increases, the deconvoluted volume fractions from both M and H converge towards almost the same value. This is illustrated in Fig. 7, displaying the convergence behavior of the relative volume fractions LD C–S–H and HD C–S–H. As one would expect, as the number N of indents increases, the sampling size of the material increases as $\ell\sqrt{N}$, with $\ell = 10\,\mu\text{m}$ the grid spacing (distance between individual indents), which is why the relative volumetric proportions converge. The extraction of volume fractions from the grid indentation technique becomes of great value in particular in cases where materials do not differ in their chemistry but rather in their morphology. In the case of C–S–H for example a quantitative X-ray diffraction analysis is incapable of detecting the two types of C–S–H and their relative volumetric proportions.

3.3. Mapping the nanostiffness properties

The analysis of each indentation curve provides information about the mechanical properties at a point of the grid. The discrete data system can then be transformed in a continuous distribution of mechanical properties by linearly interpolating the nodal values

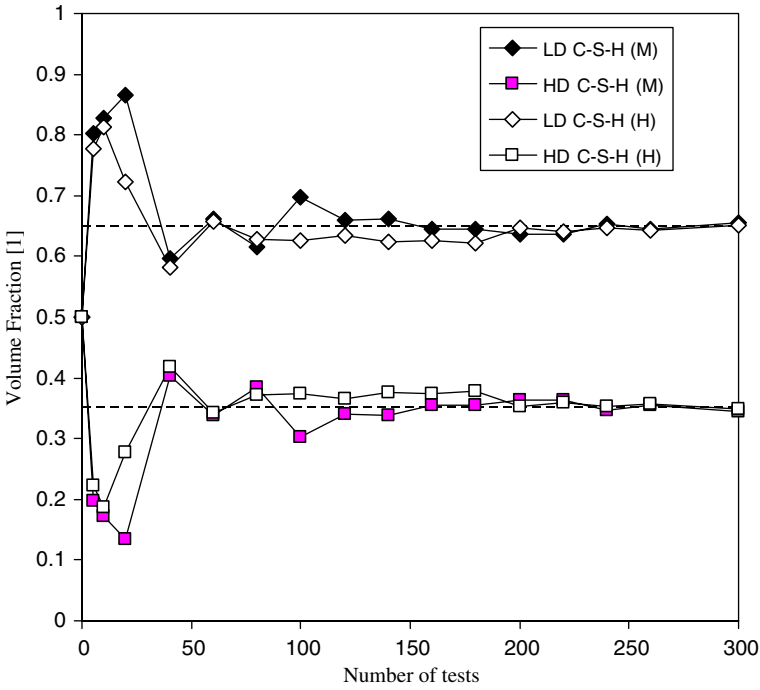

Fig. 7. Convergence of the relative volumetric proportions of LD and HD C–S–H with increasing number of indentations (or sampling area).

over the whole indented surface (grid region). This mapping of nanomechanical properties provides an additional information about the morphological arrangement of the different phases in the composite material, within the limits of the grid resolution. Indeed, the mapping is the more accurate the smaller the spacing between indents compared to the characteristic length scale of the heterogeneity. However, there is a limit to reducing the spacing which must avoid interaction between consecutive indents. Furthermore, as the frequency plots 3–6 show, there is some significant overlap in the distributions between individual phases, which makes it difficult to define clear boundaries between phases. As a first-order approach, we choose equal size domains centered around the mean values of each phase:

1. Macroporosity domain $M \in [0-13]$ GPa: Values situated in this range are associated with regions for which the indentation response is dominated by high porosity. These areas are indicative of a morphology dominated by macroporosity.
2. LD C–S–H domain $M \in [13-26]$ GPa: Values situated in this range are contained within the second peak in the frequency plots and are associated with regions in which the indentation response is dominated by the LD C–S–H.
3. HD C–S–H domain $M \in [26-39]$ GPa: Values situated in this range correspond to the third peak in the frequency plots, and are attributed to the dominant effect of the HD C–S–H.

4. CH domain and unhydrated clinker $M > 39\,\mathrm{GPa}$: The higher stiffness values are indicative of portlandite and unhydrated clinker phases. While the first tends to grow in regions of high w/c ratios adjacent to macropores and in between LD C–S–H, the residual clinker phases are generally rimmed by HD C–S–H.

Fig. 8 shows plan views of contour plots of the indentation modulus for the three series N-1, N-2 and N-3. An SEM image of a cement paste of $w/c = 0.5$ at 28 days is also shown in this figure, and demonstrates the qualitative resemblance of the mechanical maps with electron microscopy images. Hence, the mechanical maps provide a means to characterize the morphology of the microstructure at the scale defined by the chosen (nano)indentation depth, and allows visualizing microstructural features. In particular, for hardened cement paste, the contour plots provide a snapshot of the formation process of the cement paste: unhydrated clinker particles are rimmed by HD C–S–H which can be associated with the so-called IPs. Further away from high-stiffness phases is the LD C–S–H, forming OPs, which seems to be the percolated matrix phase in our $w/c = 0.5$ material system. Of great importance is also the repeatability of the microstructural features detected by mapping the mechanical properties. The three images obtained from three test series are very similar suggesting that a $100 \times 100\,\mu\mathrm{m}^2$ grid surface is able to avoid any statistical bias in the detection of microstructural features. This is consistent with the convergence of volume fractions with increasing sampling regions presented in Fig. 7.

3.4. A posteriori check of indentation invariants

The premise of the grid indentation technique and the related deconvolution technique is that it is possible to use the tools of continuum indentation analysis by carefully choosing the indentation depth. A final check of the relevance of this assumption is in order. This is achieved by evaluating the classical indentation invariants (12). Those relations hold for each indentation test performed on a homogeneous material. If we indent on a heterogeneous material, each of those invariants should actually be a discrete random variable. Hence, for an indentation on a given phase, the relations should be independent of the indentation depth, provided the scale separability condition is satisfied. In other words, an investigation of any possible scaling of those invariants provides a means to verify or falsify the separation of scale condition, on which the continuum indentation analysis is based. In checking the scaling relationships, however, one needs to separate the different phases. There is a priori no theoretical reason that the invariants for each phase should have the same value. In fact, as relations (12) show, the actual value of $\Pi_\alpha = P_{\max}/(Mh_{\max}^2)$ and $\Pi_\beta = A_c/h_{\max}^2 = P_{\max}/(Hh_{\max}^2)$ is a function of the mechanical properties of each phase $(c/M, \nu, \varphi)$ and of the indenter geometry (equivalent half-cone angle $\theta = 70.32$ for Berkovich indentation). Fig. 9 displays the invariants vs. indentation depth $h_{\max}$, and identifies data for individual phases. For reference and comparison, let us note that Berkovich indentation into a linear isotropic elastic half-space yields $\Pi_\alpha^{\mathrm{el}} = 2/\pi \tan\theta = 1.78$ and $\Pi_\beta^{\mathrm{el}} = 4/\pi \tan^2\theta = 9.95$, which are displayed as vertical straight lines in Fig. 9. The Π_α values we obtain from our experiments are all somewhat smaller than the elastic values, except for the clinker phase (CL) which has Π_α values on the same order. Similarly, our Π_β values are significantly higher than the elastic value. The most interesting observation is that the value $\Pi_\beta = 30.9 \pm 4.5$ takes for different

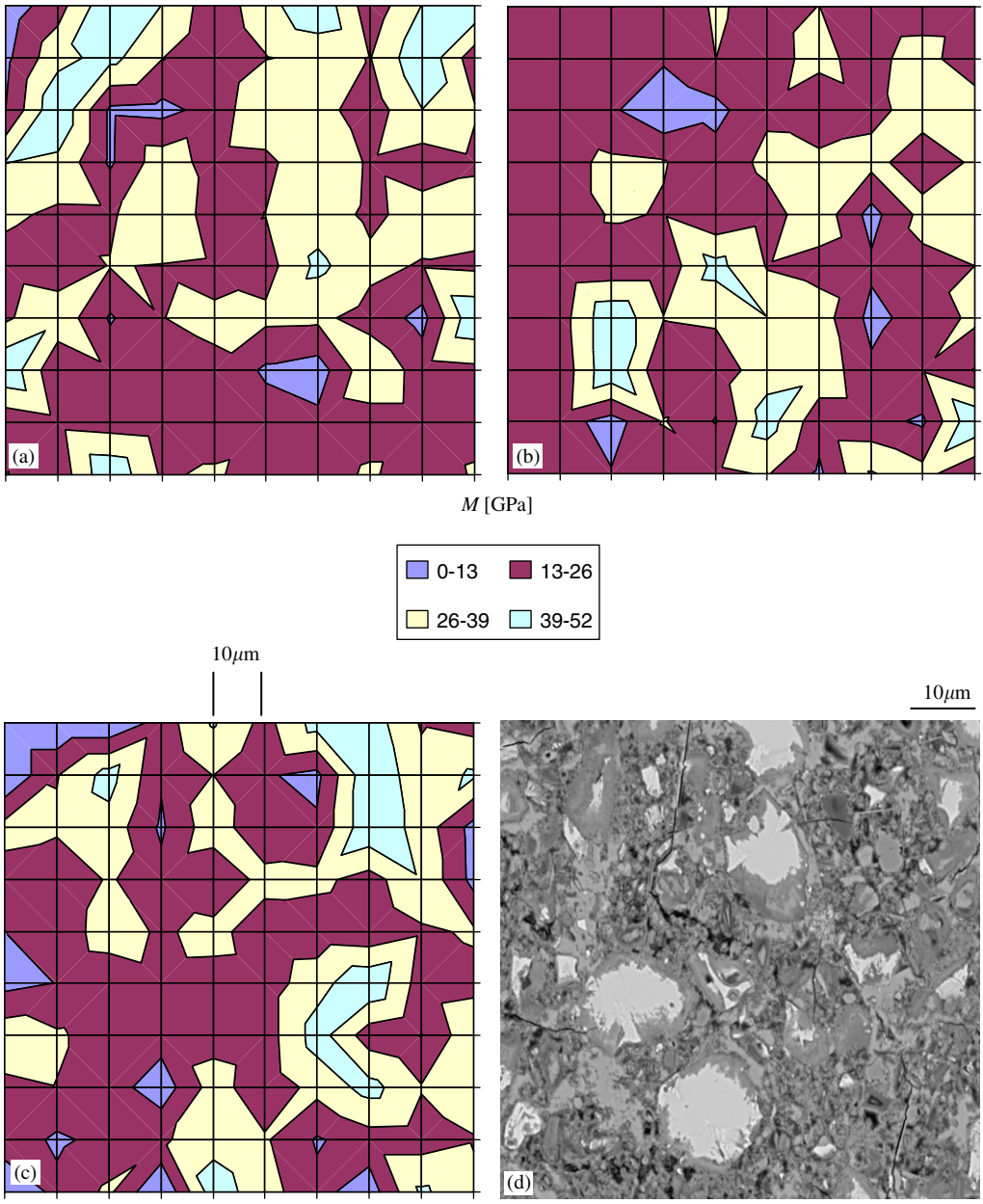

Fig. 8. Plan views of mechanical maps of indentation modulus: (a) series N-1; (b) series N-2; (c) series N-3. A similar magnification of an SEM image (d) is also shown for comparison (courtesy of K. Scrivener). Image size: $150 \times 150\,\mu m^2$; grid spacing $= 10\,\mu m$.

phases and different indentation depths does not vary in large proportions. On the other hand, the values of Π_α vary quite significantly, ranging from $\Pi_\alpha \sim 0.5$ for the MP-phase to $\Pi_\alpha \sim 1.5$ for the CL-phase. Due to local material and experimental variations

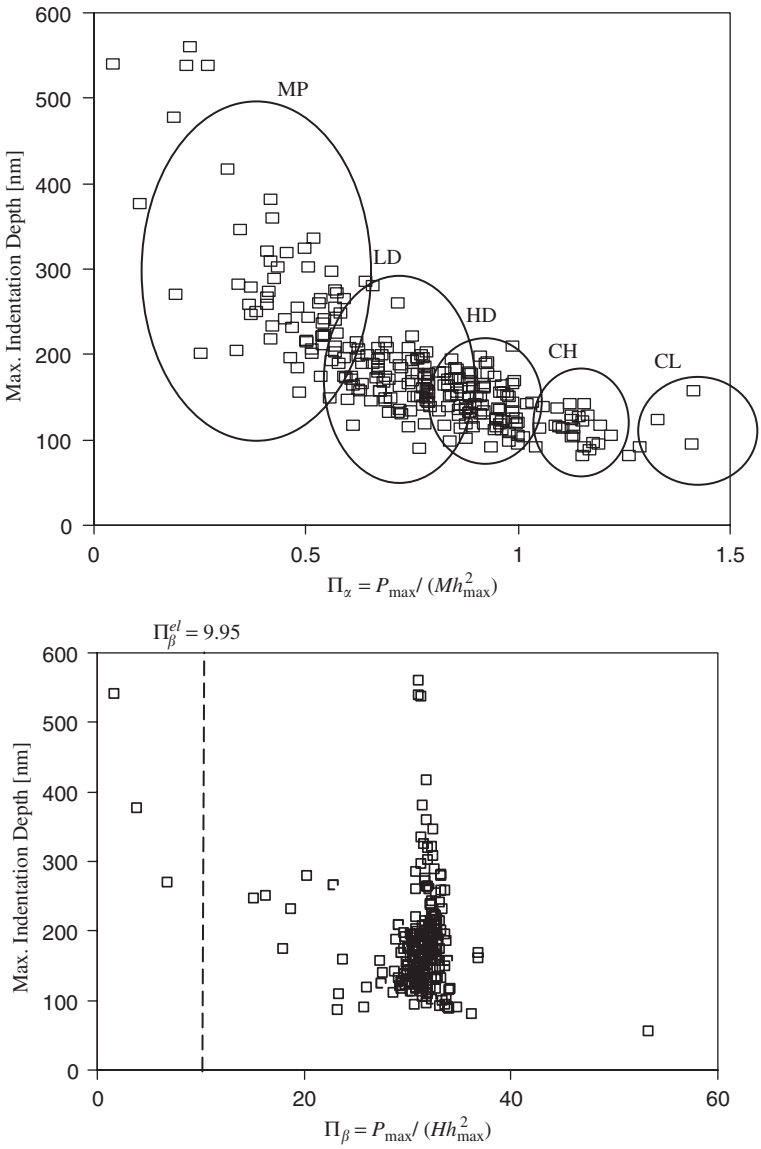

Fig. 9. A posteriori check of indentation invariants $\Pi_\alpha = P_{\max}/(Mh^2_{\max})$ and $\Pi_\beta = A_c/h^2_{\max}$: scaling relations for all test data on white cement paste. For a homogeneous material with no inherent length scale related to microstructure there should be no dependence of the invariants on the depth of indentation, corresponding in the figures to straight vertical lines. For reference and comparison, $\Pi^{el}_\alpha = 2/\pi \tan\theta = 1.78$ and $\Pi^{el}_\beta = 4/\pi \tan^2\theta = 9.95$ for Berkovich indentation into a linear isotropic elastic half-space. The outliers in the figures are indentation data from irregular test data with displacement jumps.

a scatter around the mean values is observed which is consistent with the scatter in the frequency plots in Fig. 6. In the light of Eq. (12a), it is most likely that this variation is a consequence of the cohesion-to-stiffness ratio c/M. A means of quantifying this dependence of the heterogeneous response is the indentation modulus-to-hardness ratio,

$M/H = \Pi_\beta/\Pi_\alpha$ for the different phases, J:

$$\frac{M}{H} = \begin{cases} 47.3 & \text{MP}, \\ 40.3 & \text{LD C}-\text{S}-\text{H}, \\ 35.0 & \text{HD C}-\text{S}-\text{H}, \\ 30.9 & \text{CH}, \\ 14.5 & \text{CL}. \end{cases} \tag{24}$$

Since Π_β is almost the same for all phases, M/H is a mere reflection of the variation of $1/\Pi_\alpha$. The values (24) for all phases are all greater than the elastic value $M/H = 2\tan\theta = 5.59$. The value for the residual clinker phase we obtain from our data, $(M/H)_{\text{CL}} = 14.5$ is very close to the one of pure clinker phases reported in the open literature (Velez et al., 2001): $(M/H)_{C_3S} = 15.5$, $(M/H)_{C_2S} = 16.3$, $(M/H)_{C_3A} = 13.4$ and $(M/H)_{C_4AF} = 13.2$. There is a clear difference between the M/H values of the other hydration phases, and in particular between LD C–S–H, HD C–S–H and CH, which provides some evidence that we deal here with different chemomechanical phases of different stiffness and strength properties. The M/H ratio is on-average constant per phase, providing a posteriori evidence that the deliberate choice of the indentation depth (14) leads to satisfying the scale separability condition (5).

4. Discussion

Among the key elements that allow for the assessment of the link between morphology and mechanical property is the porosity ϕ or its complimentary part the packing density, $\eta = 1 - \phi$. Unfortunately, cementitious materials have not a single porosity or a single packing mode, but at least three distinct pore spaces that are of different nature. These are from the nanoscale to the macroscale: (1) the nanoporosity of a characteristic size smaller than one nanometer, which separates C–S–H mineral layers; (2) the gel porosity contained in C–S–H gel on the order of the size of the elementary C–S–H particle, 5 nm, (3) the capillary porosity of a characteristic size of tens to a hundred nanometer. From weighting experiments, Jennings (2004) in a number of remarkable papers provides estimates of the different 'apparent' densities of cementitious materials at different scales (see Table 2), which allows one to build the following three-scale porosity model of the cement paste (Ulm et al., 2005):

$$\phi_{\text{tot}} = (\phi_0\eta_{\text{LD}} + \phi_{\text{LD}})f_{\text{LD}} + (\phi_0\eta_{\text{HD}} + \phi_{\text{HD}})f_{\text{HD}} + \phi_{\text{c}}, \tag{25}$$

where ϕ_0 is the nanoporosity, $\eta_{\text{LD}} = 1 - \phi_{\text{LD}}$ and $\eta_{\text{HD}} = 1 - \phi_{\text{HD}}$ are the packing density of the LD C–S–H and HD C–S–H, which occupy the relative C–S–H volume proportion f_{LD} and $f_{\text{HD}} = 1 - f_{\text{LD}}$, and ϕ_{c} is the capillary porosity. While f_{LD}, f_{HD} and ϕ_{c} depend on mix proportions (namely on the w/c ratio, the hydration degree, etc.; see Eq. (19)), both the nanoporosity ϕ_0 and the gel packing densities η_{LD} and η_{HD} do not vary from one cementitious material to another; instead they are intrinsic parameters characteristic of the morphology of all cementitious materials. In particular, from the density values provided by Jennings (2004) for saturated and dry C–S–H, it is straightforward to estimate the nanoporosity $\phi_0 = 0.18$, respectively, the C–S–H sheet packing density $\eta_{\text{s}} = 1 - \phi_0 = 0.82$. Similarly, the packing density of the LD C–S–H and HD C–S–H is found to be $\eta_{\text{LD}} = 0.63$ and $\eta_{\text{HD}} = 0.76$. It is intriguing to remark that these two packing densities almost coincide

with *limit* packing densities of spheres: the LD C–S–H packing density almost coincides with the random packing density of spheres of $\eta \approx 0.64$, which corresponds to the maximum packing density in the random close-packed limit (known as RCP) (Jaeger and Nagel, 1992).[2] In return, the HD C–S–H packing density almost coincides with the densest possible spherical packing in three dimensions of $\eta = \pi/\sqrt{18} \approx 0.74$ (Sloane, 1998), which is the ordered face-centered cubic (fcc) or hexagonal close-packed (hcp) packing. We will show below that this is not a pure coincidence, but a consequence of the morphology the C–S–H particles realize in situ around two characteristic packing modes one being an unstructured (random) order of the LD C–S–H the other a highly structured order of the HD C–S–H.

4.1. Link with C–S–H packing density

It is not surprising that the mechanical properties (M, H) increase with the packing density, as a matching of the nanoindentation modulus and hardness and of the characteristic packing densities in Tables 1 and 2 shows. However, as Fig. 10 shows, both indentation stiffness and hardness scale with the packing density along a straight line that yields a zero stiffness for a packing density of the C–S–H particles of $\eta \sim 0.5$. This particular behavior is a unique hallmark of granular materials. Indeed, from granular mechanics it is known that a granular assembly becomes unstable below the random loose-packed limit (RLP) of $\eta = 0.56$ (Jaeger and Nagel, 1992), which corresponds to the loosest packing of spheres for which a continuous force path can be established. The nanoindentation results, therefore, provide evidence that the two packing limits that characterize the LD C–S–H and HD C–S–H are not a coincidence, but a consequence of a nanogranular nature of C–S–H. By nanogranular nature we mean a mechanical behavior at the nanoscale of the C–S–H particles that is dominated by particle-to-particle contact, rather than by mineral properties. As the packing density increases, the number of contacts increases (Donev et al., 2004). The higher stiffness and hardness of the HD C–S–H compared to LD C–S–H, therefore, is attributable to the greater number of contact points that stabilize the particle. In particular, the hardness ratio $H_{\mathrm{HD}}/H_{\mathrm{LD}} \approx 1.8$ comes very close to the ratio of contact points: a maximum of 12 points of contacts for the ordered fcc or hcp packing (Sloane, 1998), vs. 6 points of contact for the random packing limit of spheres (Donev et al., 2004). Furthermore, an extrapolation of the $M-\eta$ and $H-\eta$ scaling relations in Fig. 10 to $\eta = 1$ provides a means to evaluate the asymptotic contact modulus, $m_{\mathrm{s}} = M(\eta = 1)$, and contact hardness, $h_{\mathrm{s}} = H(\eta = 1)$, between C–S–H particles:

$$\eta \to 1 : m_{\mathrm{s}} = 61.2\,\mathrm{GPa}, \quad h_{\mathrm{s}} = 1.78\ \mathrm{GPa}; \quad \frac{m_{\mathrm{s}}}{h_{\mathrm{s}}} = 34.4. \tag{26}$$

4.2. Complementary micromechanics analysis

Direct experimental measurement of the nanomechanical properties of the 5 nm C–S–H solid particle is still out of reach, and indeed the only measurable properties by nanoindentation are the ones of the LD C–S–H and HD C–S–H *composite*. As an alternative to the extrapolation (26), we employ, for the indentation data modeling, the

[2]More recent concepts refer to the RCP as the maximally random jammed state (MRJ), corresponding to the least ordered among all jammed packings, which has been shown to have a density of 63.7%, and which is very close to the traditional definition of the random close-packed limit; see Donev et al. (2004), and references cited herein.

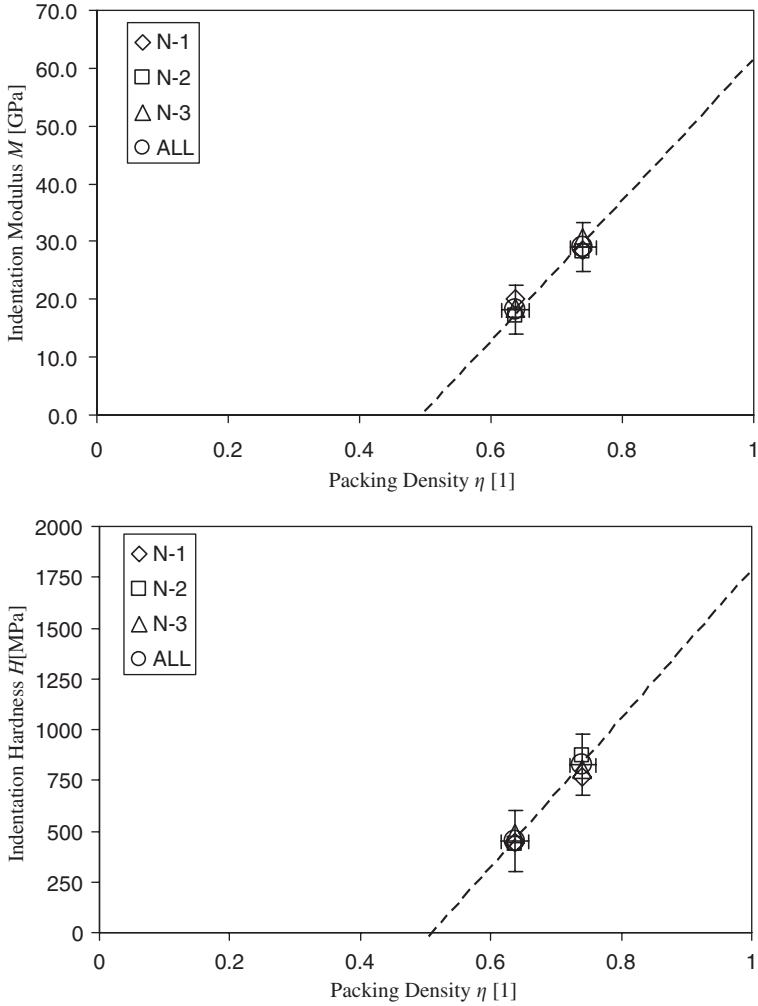

Fig. 10. Scaling of indentation modulus M and indentation hardness H with C–S–H packing density η.

tools of continuum micromechanics (Suquet, 1997; Zaoui, 2002), or more precisely those of microporomechanics (Dormieux et al., 2002; Dormieux and Ulm, 2005). The microelasticity of a porous material whose solid is a granular material, is best captured by the so-called self-consistent or polycrystal micromechanical model. Indeed, the self-consistent model of Hershey (1954) and Kröner (1958) is based on averaging the stress and strain in a spherical grain over all orientations (Kröner, 1971), and captures a morphology of a perfectly disordered solid phase intermixed with some porosity. This yields the following expressions of the bulk and shear modulus K and G of the composite:

$$\frac{K}{k_s} = \frac{4\eta G/g_s}{4G/g_s + 3(1-\eta)r_s}, \tag{27}$$

$$\frac{G}{g_s} = \frac{1}{2} - \frac{5}{4}(1-\eta) - \frac{3}{16} r_s(2+\eta) + \frac{1}{16}\sqrt{144(1-r_s) - 480\eta + 400\eta^2 + 408 r_s \eta - 120 r_s \eta^2 + 9 r_s^2 (2+\eta)^2}, \tag{28}$$

where k_s and g_s are bulk and shear modulus of the solid phase, and $r_s = k_s/g_s = 2(1+\nu_s)/3(1-2\nu_s) > 0$. As a reminder, the self-consistent scheme has a packing percolation threshold $\eta_0 = 0.5$, which is close to the RLP, for which reason it is most suitable for modeling the linear elastic behavior of granular materials. The non-negativity of the composite bulk and shear modulus is ensured for packing densities $\eta \geqslant 0.5$. Furthermore, use of (27) and (28) in (3) provides a means to evaluate the link between the composite indentation modulus M and the solid's elastic modulus m_s as a function of the composite shear modulus ratio G/g_s, the solid's bulk-to-shear modulus ratio $r_s = k_s/g_s$ and the packing density η:

$$\frac{M}{m_s} = \mathscr{F}_{sc}(\eta, r_s) = \frac{G}{g_s} \frac{(9\eta r_s + 4G/g_s + 3r_s)(3r_s+4)}{4(4G/g_s + 3r_s)(3r_s+1)}. \tag{29}$$

In particular, a solid's Poisson's ratio of $\nu_s = \frac{1}{5}$ ($r_s = \frac{4}{3}$) yields a linear scaling of all elastic properties with the packing density:

$$\frac{M}{m_s} = \mathscr{F}_{sc}(\eta, r_s = 4/3) = 2\eta - 1. \tag{30}$$

Hence, the micromechanics model provides an explanation for the linear experimental scaling in Fig. 10. In particular, it allows us to identify the asymptotic contact stiffness $m_s = M(\eta = 1)$ as the stiffness of the solid phase of the nanogranular material.

To substantiate this finding, Fig. 11 displays the indentation modulus scaling relations for two pore morphologies: the polycrystal morphology as defined by (29) and a matrix-pore inclusion morphology, which is represented in micromechanics by the Mori–Tanaka scheme (MT), and for which (Ulm et al., 2004):

$$\frac{M}{m_s} = \mathscr{F}_{mt}(\eta, r_s) = \frac{1}{4} \frac{\eta(8+9r_s)(32+300r_s+207r_s^2 - 3\eta r_s(56+33r_s))}{(3r_s+1)(24r_s - 15\eta r_s + 8)(20+15r_s - 6\eta(2+r_s))}. \tag{31}$$

In contrast to the ad hoc linear fitting of the experimental results shown in Fig. 10, the micromechanics models (29) and (31) provide a rational means to determine not only the constituent properties ($m_s, r_s = k_s/g_s$), but as well the pore morphology, captured by the solid percolation threshold η_0 ($\eta_0 = 0$ for a matrix-pore inclusion morphology, $\eta_0 = \frac{1}{2}$ for a polycrystal morphology); from minimizing the quadratic error between the experimental indentation modulus and the model values:

$$\min_{\eta_0, (m_s, r_s)} \sum_{i=\mathrm{LD,HD}} (M_i - m_s \mathscr{F}_{\eta_0}(\eta_i, r_s))^2, \tag{32}$$

where $\mathscr{F}_{\eta_0=1/2} = \mathscr{F}_{sc}$ and $\mathscr{F}_{\eta_0=0} = \mathscr{F}_{mt}$ are given by (29) and (31), respectively. Fig. 11 shows the results of the back analysis, and details are given in Table 3. The solution of the minimization problem clearly identifies the C–S–H solid phase as a polycrystal having a solid stiffness of $m_s = 60 \pm 2$ GPa. The optimal Poisson's ratio is $\nu_s = -0.08$, hinting towards a highly compressible solid phase. The micromechanics analysis thus confirms the nanogranular nature of the two C–S–H phases, LD C–S–H and HD C–S–H: comprised of

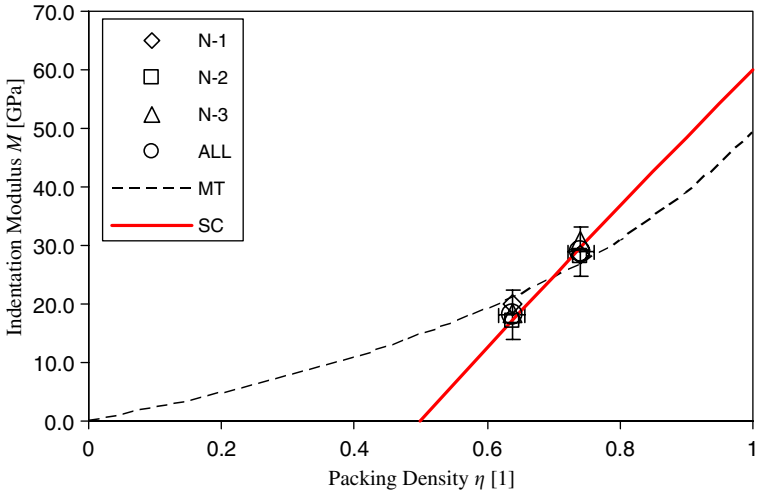

Fig. 11. Indentation modulus—packing density scaling relations for two pore morphologies: the self-consistent (SC) micromechanical model and the Mori–Tanaka (MT) matrix-pore inclusion model. Both model were fitted to minimize the error between experimental indentation values and model values. The better fit obtained with the SC-model confirms the nanogranular morphology of C–S–H.

Table 3
Results of back analysis: $m_s = C-S-H$ solid stiffness (in GPa), ν_s = solid Poisson's ratio

	Mori–Tanaka		Self-consistent	
C–S–H solid	m_s	ν_s	m_s	ν_s
N-1	50.1	0.5	60.6	−0.08
N-2	47.4	0.5	57.9	−0.08
N-3	51.3	0.5	62.7	−0.08
ALL	49.3	0.5	60.1	−0.08
Error (GPa^2)	12.3		1.5	

the same solid particle, the different mechanical performance of the two types of C–S–H is related to differences in their packing density.

Finally, it is appropriate to compare the found C–S–H solid stiffness values with an estimate of the Young's modulus of the C–S–H solid phase recently obtained from atomistic simulations. From energy minimization at 0 K, Pellenq and Van Damme (2004) reported the Young's modulus of Hamid's structure (C/S = 1) to be $E_s = 57.1$ GPa, which compares fairly well with the Young's modulus we calculate from $E_s = m_s(1-\nu_s^2) = 59.7 \pm 1.9$ GPa.

5. Closure

We have raised the question what type of morphology drives the mechanical behavior of C–S–H? Based on a novel technique of deconvoluting nanoindentation results, the overall

picture that emerges from our study is that the C–S–H behaves mechanically like a nanogranular material, whose behavior is driven by contact forces at particle-to-particle contact points, rather than by the mineral properties themselves:

1. Our results and analysis provide strong evidence for the existence of a unique C–S–H nanoparticle which forms the basic unit of material invariant properties of all cementitious materials. This nanoparticle itself is composed of several C–S–H sheets of a characteristic size in the nanometer range and an 18% nanoporosity. But rather than those sheets, it is the nanoparticle which is at the origin of the nanogranular behavior of C–S–H. It may well be that this particular behavior is a result of the hydration reactions, during which C–S–H particles precipitate randomly and percolate beyond a packing density of 50%. As the hydration proceeds, the nanogranular units touch each other, generating contact surfaces and contact points, creating in the course of this process a material whose behavior is driven by contact forces.
2. The nanogranular assembly in hardened cementitious materials exists in a large variety of densities, from below the percolation threshold of 50% to an almost solid state, which is consistent with the large surface areas of cementitious materials, as well as with pore-size distribution studies of cement-based materials. But on-average, the hydration process leads to a material whose behavior is characterized by two limit packing densities which we associate with a characteristic LD C–S–H phase and a HD C–S–H phase. It is emphasized that those packing limits are not deterministic limits in the sense that the material in the course of its creation moves towards those limit states. In fact, we see those limit packing states as the densest possible packing that is achieved in the course of the random generation of nanoparticles during hydration. Each phase, LD C–S–H and HD C–S–H, spans some range of densities, as testified by the standard deviations, with a mean centered around, respectively, the random packing limit ($\eta = 64\%$) and the cubic or hexagonal close packing ($\eta = 74\%$) of spheres.

Finally, one may raise the question whether the C–S–H particles are actually spherical or not? Our nanoindentation technique being a statistical one, clearly cannot answer this question. However, if we remind ourselves that the 'sphere' is the easiest 'isotropic' morphology, then its successful application to C–S–H demonstrated here, hints towards an amorphous structure of C–S–H that determines the average nanomechanical response of C–S–H. While we cannot (and do not want to) exclude other morphologies, there is little doubt that those morphological features play on-average a second-order effect on the stiffness and strength behavior of C–S–H.

Acknowledgments

We are grateful for the financial support of this study by Lafarge Corporation with Jean-François Batoz as Technical Advisor and Dr. Paul Acker as Scientific Advisor. The tested materials were provided by the team of Profs. Hamlin Jennings and Jeffrey Thomas from Northwestern University, Evanston, Illinois, whose advice and suggestions are gratefully acknowledged. The nanoindentation tests were carried out in MIT's Nanolab facilities of the Department of Materials Science and Engineering, under the supervision of Alan Schwartzman and Prof. Krystyn Van Vliet.

References

Acker, P., 2001. Micromechanical analysis of creep and shrinkage mechanisms. In: Ulm, F.-J., Bazant, Z.P., Wittmann, F.H. (Eds.), Creep, Shrinkage and Durability Mechanics of Concrete and other Quasi-brittle Materials. Elsevier, Oxford, UK, Cambridge, MA.

Buckle, H., 1973. In: J.W. Westbrook, H. Conrad (Eds.), The Science of Hardness Testing and its Applications. American Society for Metals, Metal Park, OH, pp. 453–491.

Cheng, Y.-T., Cheng, C.-M., 2004. Scaling, dimensional analysis and indentation measurements. Mater. Sci. Eng. R. 44, 91–149.

Constantinides, G., Ulm, F.-J., 2004. The effect of two types of C–S–H on the elasticity of cement-based materials: results from nanoindentation and micromechanical modeling. Cem. Concr. Res. 34 (1), 67–80.

Constantinides, G., Ulm, F.-J., van Vliet, K.J., 2003. On the use of nanoindentation for cementitious materials. Mater. Struct. RILEM (205) 191–196 (Special issue of Concrete Science and Engineering).

Donev, A., Cisse, I., Sachs, D., Variano, E.A., Stillinger, F.H., Connely, R., Torquato, S., Chaikin, P.M., 2004. Improving the density of jammed disordered packings using ellipsoids. Science 303, 990–993.

Dormieux, L., Ulm, F.-J. (Eds.), 2005. Applied micromechanics of porous materials. CISM Courses and Lectures, vol. 480. Springer, Wiely, New York.

Dormieux, L., Molinari, A., Kondo, D., 2002. Micromechanical approach to the behaviour of poroelastic materials. J. Mech. Phys. Solids 50, 2203–2223.

Durst, K., Goken, M., Vehoff, H., 2004. Finite element study for nanoindentation measurements on two-phase materials. J. Mater. Res. 19 (1), 85–93.

Galin, L.A., 1961. In: I.N. Sneddon (Ed.), Contact Problems in Theory of Elasticity (H. Moss, Trans.). North Carolina State College.

Ganneau, F.P., Constantinides, G., Ulm, F.-J., 2006. Dual-indentation technique for the assessment of strength properties of cohesive-frictional material. Int. J. Solids Struct. 43, 1727–1745.

Hershey, A., 1954. The elasticity of an isotropic aggregate of anisotropic cubic crystals. J. Appl. Mech. (ASME) 21, 236–240.

Jaeger, H.M., Nagel, S.R., 1992. Physics of granular state. Science 255 (5051), 1523–1531.

Jennings, H.M., 2000. A model for the microstructure of calcium silicate hydrate in cement paste. Cem. Concr. Res. 30, 101–116.

Jennings, H.M., 2004. Colloid model of C–S–H and implications to the problem of creep and shrinkage. Mater. Struct. 37 (265), 59–70 (Special issue of Concrete Science and Engineering).

Jennings, H.M., Thomas, J.J., Gevrenov J.S., Constantinides G., Ulm, F.-J., 2006. A multi-technique investigation of the nanoporosity of cement paste. Cement Concrete Research, in Press. Online version available May 11, 2006.

Kröner, E., 1958. Computation of the elastic constants of a polycrystal from the constants of the monocrystal. Z. Phys. 151, 504–518, (in German).

Kröner, E., 1971. Statistical continuum mechanics. CISM Courses and Lectures, vol. 92. Udine, Italy.

Nonat, A., 2004. The structure and stoichiometry of C–S–H. Cem. Concr. Res. 34, 1521–1528.

Oliver, W.C., Pharr, G.M., 1992. An improved technique for determining hardness and elastic modulus using load and displacement sensing indentation experiments. J. Mater. Res. 7 (6), 1564–1583.

Oliver, W.C., Pharr, G.M., 2004. Measurement of hardness and elastic modulus by instrumented indentation: advances in understanding and refinements to methodology. J. Mater. Res. 19, 3–20.

Pellenq, R.J.M., Van Damme, H., 2004. Why does concrete set? The nature of cohesion forces in hardened cement-based materials. MRS Bull. 29 (5), 319–323.

Powers, T.C., Brownyard, T.L., 1948. Studies of the physical properties of hardened portlandite cement paste. PCA Bull. 22.

Richardson, I.G., 2004. Tobermorite/jennite- and tobermorite/calcium hydroxide-based models for the structure of C–S–H: applicability to hardened pastes of tricalcium silicate, β-dicalcium silicate, portland cement, and blends of portland cement with blast-furnace slag metakaolin or silica fume. Cem. Concr. Res. 34, 1733–1777.

Sloane, N.J.A., 1998. Kepler's conjecture confirmed. Nature 395, 435–436.

Sneddon, I.N., 1965. The relation between load and penetration in the axi-symmetric Boussinesq problem for a punch of arbitrary profile. Int. J. Eng. Sci. 3, 47–57.

Stutzman, Paul, E., Clifton, J.R., 1999. Specimen preparation for scanning electron microscopy. In: Jany, L., Nisperos, A. (Eds.), Proceedings of the 21st International Conference on Cement Microscopy, Las Vegas, Nevada, pp. 10–22.

Suquet, P. (Ed.), 1997. Continuum micromechanics. CISM Courses and Lectures, vol. 377. Springer, Wien, New York.

Tennis, P.D., Jennings, H.M., 2000. A model for two types of calcium silicate hydrate in the microstructure of portland cement pastes. Cem. Concr. Res. 30, 855–863.

Thomas, J.J., Jennings, H.M., 2002. Effect of heat treatment on the pore structure and drying shrinkage behavior of hydrated cement paste. J. Am. Ceram. Soc. 85 (9), 2293–2298.

Ulm, F.-J., Constantinides, G., Heukamp, F.H., 2004. Is concrete a poromechanics material?—A multiscale investigation of poroelastic properties'. Mater. Struct. 37 (265), 43–58 (Special issue of Concrete Science and Engineering).

Ulm, F.-J., Delafargue, A., Constantinides, G., 2005. Experimental is microporomechanics. In: Dormieux, L., Ulm, F.-J. (Eds.), Applied Micromechanics of Porous Materials. CISM Courses and Lectures, vol. 480. Springer, Wien, New York, pp. 207–288.

Velez, K., Maximilien, S., Damidot, D., Fantozzi, G., Sorrentino, F., 2001. Determination by nanoindentation of elastic modulus and hardness of pure constituents of portland cement clinker. Cem. Concr. Res. 31 (4), 555–561.

Zaoui, A., 2002. Continuum micromechanics: survey. J. Eng. Mech. (ASCE) 128 (8), 808–816.